Apr 22nd, 12:00 PM - 1:10 PM

AN INTRODUCTORY INVESTIGATION OF DUST DEVILS ON MARS: COMPUTATIONAL FLUID DYNAMICS MODELING

Alexios Nicolas Philippou
University of Glasgow

Kakkattukuzhy M. Issac
Missouri University of Science and Technology, isaac@mst.edu

AN INTRODUCTORY INVESTIGATION OF DUST DEVILS ON MARS: COMPUTATIONAL FLUID DYNAMICS MODELING

Alexios Nicolas Philippou
University of Glasgow
K. M. Isaac
Missouri University of Science & Technology

Abstract

This report investigates the flow characteristics of tornado like vortices which can be used to describe an array of axisymmetric rotating vertical columns of fluid such as dust devils, steam devils and tornadoes. These vortices have been recreated within vortex chambers in research facilities, but in focus of this report the investigation is conducted through numerical simulations using the Computational Fluid Dynamics (CFD) software package provided by ANSYS. By varying the main governing non-dimensional parameter of swirl ratio through the computational domain's boundary conditions, different flow characteristics appear which confirm theories presented in previous papers. This enables the research conducted in this report to be used as a template for further, more in-depth, investigations for different circumstances such as dust devils on Mars with their associated different conditions including gas composition, presence of possible liquid and solid phases, pressure, and temperature.

1.0 Introduction

Tornadoes are a natural phenomenon which consist of violently rotating columns of air, or vortex flows which can exceed 100m/s near the surface. This can cause catastrophic events to infrastructure within their vicinity. On a smaller scale, 'dust devils' form in a similar manner and have similar characteristics with smaller velocities. Mobile doppler radars have recorded peak azimuthal velocity components of dust devils in Texas to be about 10m/s as presented in (Bluestein, 2004)[1]. Although dust devils may not reach the high velocities of tornadoes, they may still cause considerable damage in certain situations where sensitive hardware may be at stake. For example, the Perseverance rover sent to Mars by NASA had its wind sensor damaged by a dust devil. Investigation of the genesis and progression of tornado-like flows is therefore necessary to better understand when and how these vortices are formed so that precautions may be taken against them on any scale and on any planet.

As stated in (Lewellen, 1993)[2], the key element of a tornado-like vortex flow is the convergence of ambient, axial vorticity. This element enables a broader range of vortices to be investigated, including dust-devils (Idso, 1974)[3] and waterspouts (Golden, 1971)[4]. In general, a dust devil forms by a flow which spirals radially inward into the core of the vortex. This core is essentially a rising swirling plume of fluid which may also include a downward jet along the vertical axis of rotation, depending on the swirl ratio which is a non-dimensional parameter. The closer to the ground, the more the radial and tangential flow are intensified. In large scale tornadoes, the vortex enables a large fraction of potential energy of the parent storm to be converted into kinetic energy within the wind very close to the surface where it can cause great damage to buildings and infrastructure. In a similar manner, dust devils have their highest velocities present near the ground which may also be highly damaging to smaller structures and vehicles such as rovers.

The features associated with these twisting columns of fluid flows with intense particle concentration gradients make them easily visible to the human eye, from tornadoes to dust

devils, there are a vast amount of video recordings and photographs available for all types of vortex-like flows. There has even been video evidence of the naturally occurring dust devils on the surface of Mars, by the Perseverance rover. The clear characteristic of a twirling plume of fluid with particle debris can be observed on figure 1, a direct snapshot from the Perseverance's right navigation camera's footage (NASA/JPL-Caltech, April 13, 2021)[5] taken on April 13, 2021. The funnel dust boundary visible does not denote a streamline, rather corresponds to a constant pressure surface. The sharp boundaries also suggest that the level of turbulence in the core flow is low. The Rover's companion, Ingenuity, a coaxial rotor helicopter, can be seen in the picture and can be used for reference to estimate the size of the dust devil. Ingenuity is a very small helicopter, coming in at a height of 48cm. As rough approximation, the dust devil's average region of core flow could have a diameter of 0.5m - 3.0m. Note that this is a crude estimate, and these dust devils have been recorded to vary in size. This approximation will aid in the selection of domain size for calculations which will be discussed in this paper amongst further work that can be conducted.

Investigating the fluid flow dynamics of tornadoes and smaller 'dust devils' requires a recreation of these uncontrollable spinning columns of fluid in much more controlled and predetermined domain such as laboratory scale vortex chamber with the necessary boundary conditions for their genesis. This method requires specialized facilities with high operational costs, as such, a different method will be used for this investigation. With the use of numerical simulations, we can emulate these vortex chambers and their experimental vortices at a much smaller cost. This method also allows wiggle room for simulation objectives to be varied and different points of the flow to be analyzed. The region of interest for engineering purposes is closest to the ground, where the highest speeds are present which can cause the most havoc.

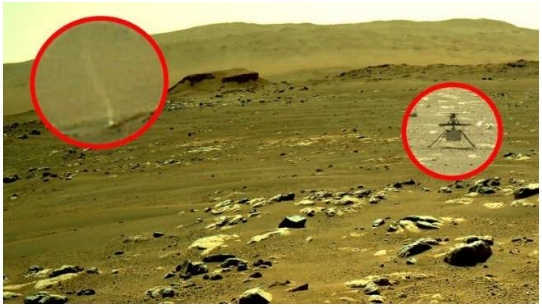

Figure 1. NASA's Perseverance rover's Ingenuity helicopter pictured with a dust devil on the surface of Mars on April 13, 2021

Given the wide array of Tornado Vortex Chambers (TVC) which have been used for experiments,(Davies-Jones R. P., 1976)[6] concluded that the Ward-type TVC (Ward, 1972)[7] presents both dynamic and geometric similarity to naturally occurring vortices. It consists of two cylindrical chambers placed one top of the other and separated by a partition plane. The lower chamber sidewall is the inlet of the chamber, this is where a rotating screen provides angular momentum to the flow. The ceiling of the upper chamber consists of a flow straightening grid and a fan to pull air out of the chamber. By altering the volume flow through the chamber and the angular momentum through the inlet region, this model can produce tornadolike flow characteristics, such as single celled, two-celled, or even multiple celled vortex configurations. As this is a rather simple, well researched model, it is a good template to begin investigations of CFD tornadoes and dust devils. A sketch of the Ward type TVC which will be modelled in CFD can be seen in figure 2.

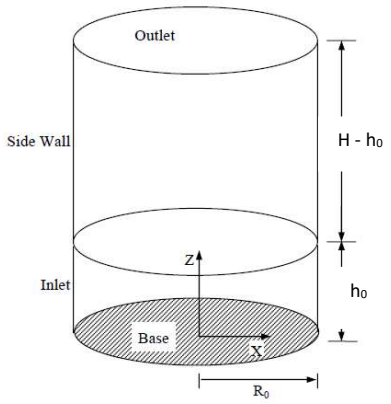

Figure 2. Ward-type TVC modelled in CFD simulations

1.1 Essential Non-Dimensional Parameters

Through extensive research specifically for tornado-like vortices,(Lewellen, 1962)[8] and (Davies-Jones R. P., 1973)[9] have alluded that the key non-dimensional parameters which govern flow characteristics are Swirl ratio (S), aspect ratio (A), Reynolds number (Re) and Froude number (Fr). The investigation presented in this report focuses upon some of these parameters and their relationship with dust devil formation. Their definitions are as follows, starting with aspect ratio:

$$A = h_0/H \tag{1.0}$$

A measure of the inlet height of the domain over the entire domain height, this will remain constant in the simulations that follow. The sketch in Figure 2 also shows these parameters.
Swirl ratio:

$$S = \frac{V_\theta}{2AV_r} \tag{1.1}$$

A ratio of tangential inflow velocity over radial inflow velocity. This will be altered in the simulations that follow.
Mach number:

$$M = v_0/a \tag{1.3}$$

The Mach number is the ratio of flow velocity magnitude over the local speed of sound. An essential parameter when considering flows in different regimes. For the study within this report, it will be used to ensure all simulations are executed within the incompressible regime. (Fiedler, 1997)[10] observed that even if the fluid used for the tornadolike flows does become compressible, the simulation results alluded that even at subsonic flow, compressibility only slightly decreases the peak wind speeds. (Xia, 2003)[11] further extended the (Fiedler, 1997)[10] research and found that compressibility effects are unlikely to alter the basic dynamics of these flows close to the surface.
Reynolds number:

$$Re = \frac{\rho v_0 R_0}{\mu} = \frac{v_0 R_0}{v} \tag{1.4}$$

Most definitely an important parameter, the Reynolds number gives an indication of whether the fluid flow investigated is laminar or turbulent. It is expressed as a ratio of inertial forces to viscous forces. Various papers, including (Rotunno, 1979)[12], state that the vortex core size is a function of swirl ratio and almost independent of the Reynolds number. This had also previously been investigated in papers such as (Ward, 1972)[7] and had therefore further been confirmed.

1.2 Vortex Flow Regions and Theory

For convenience, it is suggested to divide the flow into four distinct regions as described by Lewellen's first review (Lewellen, 1976)[8]: region (I), the core flow; region (II), the surface boundary layer flow; region (III), the central corner flow; and region (IV), the top layer. These will aid in the understanding of these vortex structures. Out of these four regions, three can be seen in figure 1. The top layer flow is not clearly defined, but regardless of this, the central corner (III) flow region is that of present interest. In this region the maximum velocities occur, and the flow dynamics are the boldest.

Firstly, in region (I), the core flow includes vortices which naturally converge upwards due to updrafts. The conservation of angular momentum with regards to the center of the updrafts intensifies any ambient vertical vorticity. In terms of fundamental fluid dynamics theory, with reference to the Kelvin-Helmholtz Theorem, the circulation within a close curve, i.e. the vortex core composed of a set of fluid particles, remains constant as the curve moves with the fluid. Consequently, if the enclosed area reduces, the vorticity increases. The existing vortex tubes in dust devils and tornadoes are stretched such that the cross-sectional area becomes smaller near the ground leading to an amplification of vorticity to keep the product of cross-sectional area and vorticity constant and hence circulation constant.

$$\oint \boldsymbol{\omega} \cdot d\boldsymbol{S} = constant = 0 \tag{2.0}$$

The surface integral helps the understanding of the Kelvin-Helmholtz's Theorems where dS is an outward directed surface element and ω is the vorticity vector. Note that this is only a qualitative description of the vortex behavior due to the assumptions underlying the Kelvin-Helmholtz Theorems.

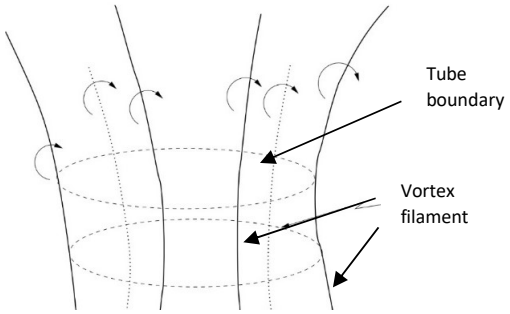

Figure 3 - Vortex filaments forming a vertically downwards converging tube similarly to dust devils

Secondly, the surface boundary layer flow, region (II), will be considered. The presence of a solid surface boundary implies a constraint on the turbulence. This leads to the momentum flux remaining constant in the wall region whilst the velocity decreases with a logarithmic rate closer to the surface. In the CFD simulations of this report, the inflow boundary region is given a constant velocity and the boundary layer develops on the ground in the simulations due to the no-slip surface boundary condition.

Thirdly, the corner flow, region (III), is where the most intriguing characteristics occur. In this region the radial flow must turn and induce a vertical jet, this happens around the centre of vortex near where the radius equals zero. The fraction of the volume flow that has been diverted to the boundary layer is what consequently defines the structure of this jet. The Swirl ratio, *S*, is ultimately what determines this relative fraction of volume flow. An array of plots with varying swirl ratio can be seen in figure 4 taken from (Davies-Jones R. , 1986)[13]. As *S* increases, the vortex transitions from a jet-like flow to a single-cell laminar vortex, increasing the parameter further results in a stagnation point and a vortex breakdown. This vortex breakdown then transitions upstream with an increasing *S*, leading to the formation of a two-cell vortex. At very high swirl ratios, a multitude of vortices appear to rotate around a parent vortex core.

Lastly, the upper flow region (IV), includes the top boundary which in tornado like vortices contains many uncertainties. In tornado research, this region is buried in the parent storm. For the simulations of this report, the common solution for this problem will be emulated. A baffle, or a vent acts as an exhaust or a pressure outlet for the domain. This region, although important for the development of different characteristics of the vortex flow, will not be a focus of interest in this paper.

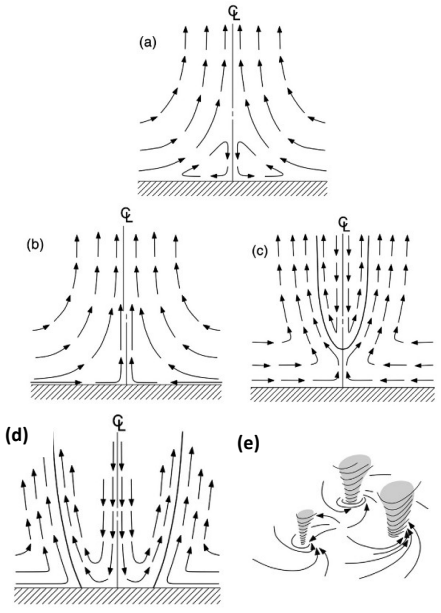

Figure 4 - The effects of increasing non-dimensional governing parameter Swirl Ratio, S, on vortex flows, (a) Very weak S - such that the boundary layer separates, (b) Low S - weak one-cell smooth flowing vortex, (c) Moderate S - vortex breakdown above the surface, (d) High S - Stagnation point transitions upstream, two-celled vortex with downdraft reaching the surface, (e) Very high S - multitude of vortices rotating around parent vortex

2.0 Solution methods and numerical setup

The Navier-Strokes equations are a set of partial differential equations that describe the dynamics of any viscous fluid. These equations mathematically express the conservation of mass through the continuity equation, and Newton's second law. To perform the fluid dynamic simulations that are presented, these equations need to be solved through CFD algorithm such that the results of the fluid motion and characteristics can develop over the entire domain. For simplicity and time efficiency, this study was conducted with the SIMPLE numerical solver. Furthermore, the Spalart-Allmaras turbulence model was chosen, as it is a widely used model with a single turbulence equation to be solved, allowing for simulations to run at a faster rate.

2.1 Computational Domain

The computational domain created in this study was constructed to emulate the Ward-type Tornado Vortex Chamber as previously mentioned. It was initially created in ANSYS 'SpaceClaim' where a circle of 6m diameter was sketched on the 'xy' plane and then extruded to a height of 6m in the 'z' direction, then split into two bodies at 10% of the total height. Although the size of the chamber is not of great importance, the design is a 6m-by-6m cylindrical chamber such that the vortices generated are to be within the range of magnitudes that dust devils may have. A crucial step in the creation of the domain during pre-meshing, is ensuring that shared topology is declared between the two circular interfaces of the top and bottom cylinders.

The two chambers were listed under a single component and imported into the ANSYS Mesher. For the CFD simulations to be executed with certain acceptable accuracy whilst attempting to be time-efficient, a mesh size of approximately 1,500,000 cells was initially created. The mesh type was 'unstructured' consisting of tetrahedrons. A sizing parameter was created for the entire domain with a line size of 0.12m. A multitude of previous research papers has alluded that the most interesting fluid characteristics develop near the surface, and as such it is important to create an inflation layer near the bottom surface (ground). This section of refined mesh will ensure a gradual increase in cell size from the ground up to a height of approximately 30cm ensuring that any interaction on the surface that may affect the entire vortex is captured. The choice of parameters results in the mesh of 1,634,238 cells as seen in figure5.

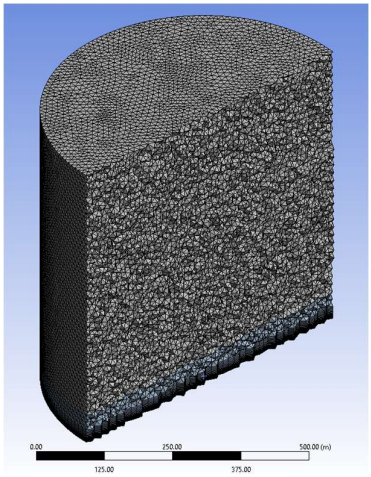

Figure 5 - Mesh of the TVC domain cross-section

Following the creation of the mesh, the pre-processing procedure requires named selections to be specified along all outer surfaces of the domain. This ensures that boundary conditions can be declared on all outer surfaces. The mesh is then imported into the ANSYS Setup window, where boundary conditions are specified and the flow solver in a transient solution can be selected. One common solver option, among others, is called SIMPLE. Referring to figure 5, a simple schematic of the domain is shown with all boundary condition declarations. It is important to note that a detailed mesh snapshot of the highlighted region enclosed in the figure is given in the Appendix where the inflation layer can easily be seen.

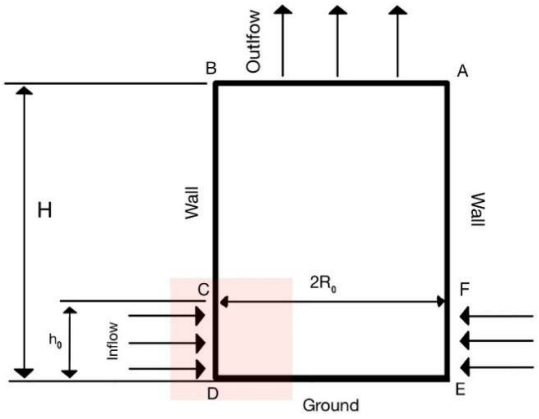

Figure 6. Domain schematic with labelled boundary conditions

Surface	Boundary type	Parameters and Setting declarations
A-B	Pressure-outlet	Gauge pressure = 0 Prevent Reversed flow selected
B-C F-E	Wall	Roughness Constant = 0.0005 Roughness height = 0.0001m
C-D E-F	Velocity Inlet	Radial and tangential velocity altered in simulations
D-E	Wall	Roughness Constant = 0.5 Roughness height = 0.01m No-slip condition applied

Table 1. Associated boundary conditions with reference to Figure 5

Run	Swirl Ratio	Velocity Magnitude (m/s)	Mach number	Reynolds number
1	0.2	7	0.021	1,173,578
2	0.6	7	0.021	1,173,578
3	2.0	7	0.021	1,173,578
4	0.6	70	0.206	11,735,777

Table 2. Simulation runs with associated input velocities and parameters

2.1 Results and discussion

In this section, results from the simulations at t = 60 s from the start are discussed. Figures 7.1 to 7.4 show the static pressure contours for the conditions as follows: 7.1: V = 7 m/s, S = 0.2, 7.2: V = 7 m/s, S = 0.6, 7.3: V = 7 m/s, S = 2, and 7.4: V = 70 m/s, S = 0.6. These were chosen to study the effect of swirl ratio and the Reynolds number which is higher by a factor of 10 for the case in Fig. 7.4. The pressure contours in these figures are in the xz-plane. In Fig. 7.1, the pressure is the highest near the ground toward the center indicated by the red triangular regions to either side of the z-axis. For all the 4 cases, the pressure is lower near the axis compared to locations at larger radii. The negative pressure magnitude is highest in the elongated bubble indicated in blue (Fig. 7.1).

As the swirl ratio is increased to S = 0.6 (Fig. 7.2), the pressure contours show significant differences from the S = 0.2 case. It ranges from -108 Pa to 16 Pa. The low pressure region is smaller and closer to the ground, and does not have a full oval shape. The highest pressure region also occurs near the ground near r = 0. Aformentioned as the corner flow region, this is where radial flow turns and induces a vertical jet. With increasing swirl ratio, the conrer flow region moves away from the center as the lower pressure region begins to dominate near the central surface region.

As the swirl ratio is further increased to S = 2, the contours are as shown in Fig. 7.3. The range is -37 Pa to 25 Pa. There is a large negative pressure region that extends from the ground to nearly half the height of the domain. The negative pressure gradient toward the ground along the axis would induce a downward flow at the center confirming observations of some natural tornadoes. This supports the theory presented in (Davies-Jones R. , 1986)[13], as with increasing Swirl, the stagnation point transitions upstream until it reaches the surface and vortex breakdown occurs creating a two-vortex flow.

Figures 7.1, 7.2 and 7.3 together help understand how the swirl ratio affects the flow pattern. As S increases, the oval-shaped low pressure region moves toward the ground and transitions to an incomplete oval at S = 0.6. At S = 2, the high pressure region near the ground indicated in red has become smaller, and the flow field still has a high degree of axial symmetry.

In Fig. 7.4, the velocity is higher by a factor of 10 compared to the first three cases, and the swirl ratio S = 0.6. This case helps to understand the effect of Reynolds number on the flow field. The corresponding increase in *Re* by a factor of 10, changes the flow field significantly. The first observable change is the loss of symmetry about the z-axis. In contrast, the present results based on 3D simulations show a high degree of axial symmetry in Figs. 7.1 to 7.3. A direct comparison can be made between Figs. 7.2 and 7.4, which differ only in the velocity, and hence the Reynolds number. Thus the loss of symmetry can be attributed to the higher Reynolds number in Fig. 7.4, where the flow is more turbulent.

Figure 8 shows pressure contours in the xy-plane close to the ground at z = 10 cm. This plane was chosen to understand the flow field behavior near the ground as the flow with uniform velocity at the inlet interacts with the ground, and the boundary layer develops. The contours in Fig. 8.3 show some asymmetry in the azimuthal direction in the inner low pressure region. However, in Fig. 8.4 for the higher *Re* case, there is greater symmetry. One likely explanation for this behavior might lie in the turbulence model. More study of the Spalrt-Almaras turbulence model for flows with high degree of swirl could shed more light on this behavior. At V = 7 m/s, $Re_{r0} = 1.419 \times 10^6$, and at V = 70 m/s, $Re_{r0} = 14.19 \times 10^6$. This factor of 10 difference in the Reynolds number could be another reason for the pressure contours having greater

symmetry in the xy plane at z = 10 cm, in Fig. 8.4. The turbulent boundary layer thickness can be estimated at r_0 = 1 m, the radius where pressure asymmetry is clearly seen. They are δ_{r0} = 2.18 cm for the lower *Re* case, and δ_{r0} = 1.37 cm for the higher *Re* case. Therefore, in both cases the z = 10 cm plane is well outside the boundary layer.

Figure 9 shows velocity vectors and velocity contours in the xz plane for S = 0.2, 0.6 and 2, respectively. Close to the ground, the radial velocity magnitude v_r decreases and the axial velocity magnitude v_z increases toward the axis in accordance with the continuity equation. A large recirculation region is present on the side wall, which changes shape and size with the swirl ratio. For the higher *Re* case in Fig. 9.4, the loss of symmetry is present as observed in the pressure contours in Fig. 7.4. At the swirl ratio S = 0.6, the downward flow begins to appear (Fig. 9.2) and grows even stronger for S = 2 (Fig. 9.3). It is evident that at S = 2, vortex breakdown fully occurs resulting in a two celled vortex formation suggested by the two closed vector loops. The axial flow is less organized in the higher *Re* case (Fig. 9.4), most likely due to the loss of symmetry in the axial plane.

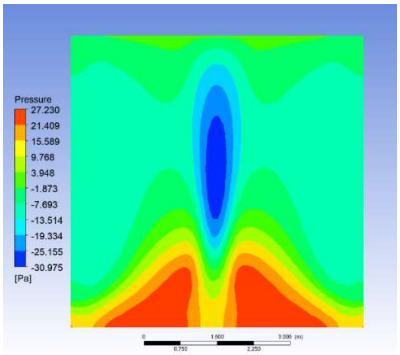

7.1. Run 1, S = 0.2, V = 7.0m/s

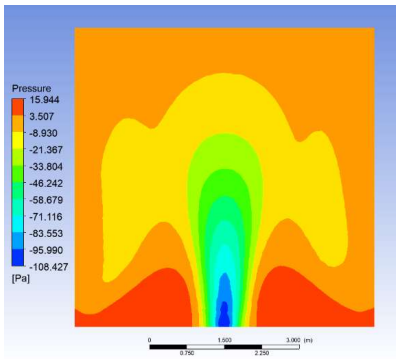

7.2. Run 2, S = 0.6, V = 7.0m/s

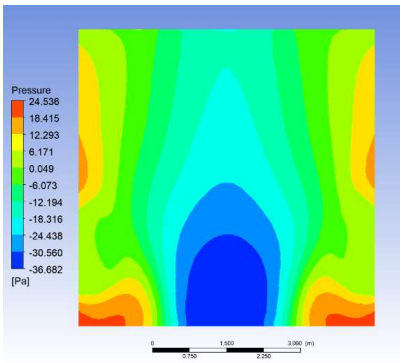

7.3. Run 3, S = 2.0, V = 7.0m/s

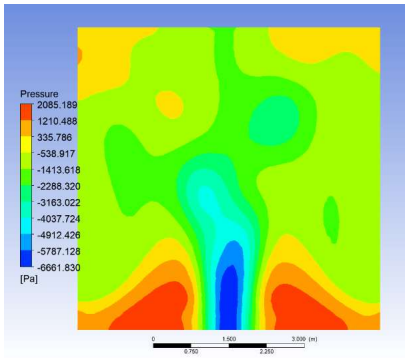

7.4. Run 4, S = 0.6, V = 70.0m/s

Figure 7. Pressure contours along XZ axial cross-section of domain

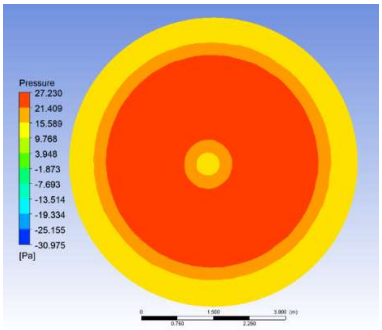

8.1. Run 1, S = 0.2, V = 7.0m/s

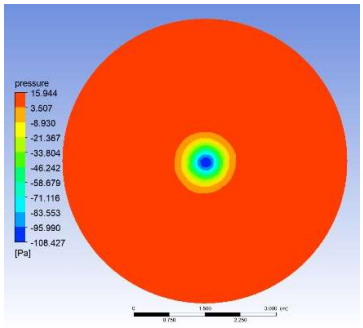

8.2. Run 2, S = 0.6, V = 7.0m/s

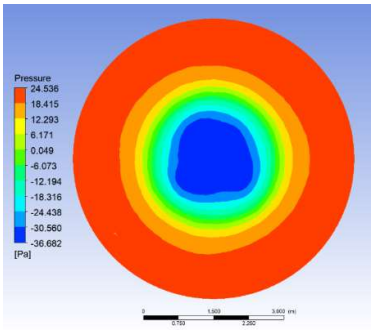

8.3. Run 3, S = 2.0, V = 7.0m/s

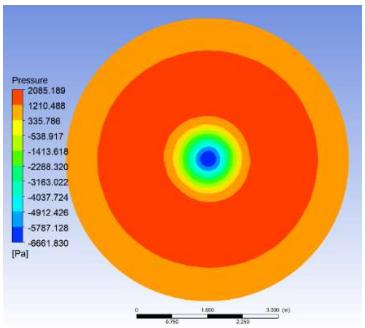

8.4. Run 4, S = 0.6, V = 70.0m/s

Figure 8. Pressure profiles along cross-section of domain at a height of 10cm in the XY plane

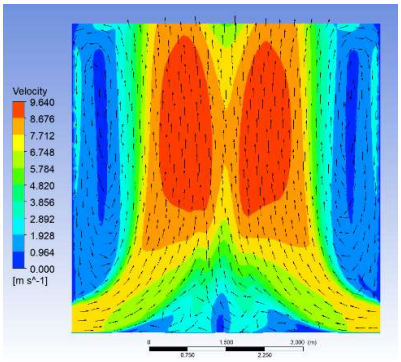

9.1. Run 1, S = 0.2, V = 7.0m/s

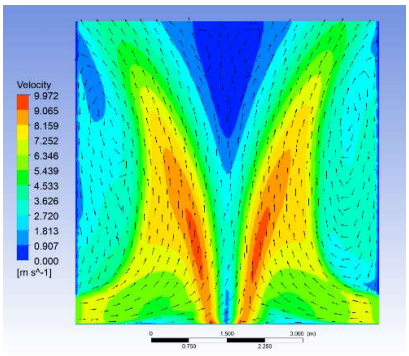

9.2. Run 2, S = 0.6, V = 7.0m/s

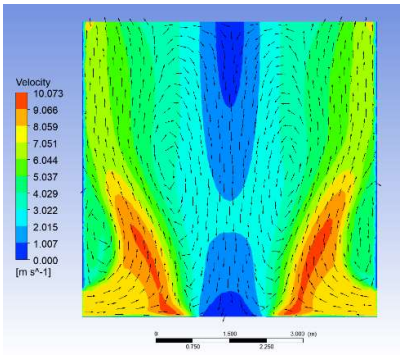

9.3. Run 3, S = 2.0, V = 7.0m/s

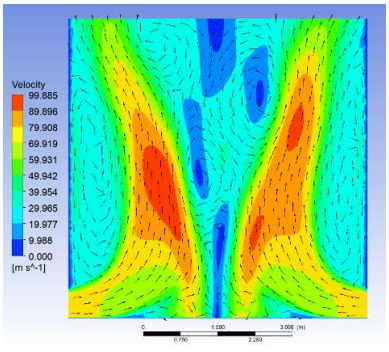

9.4. Run 4, S = 0.6, V = 70.0m/s

Figure 9. Velocity contours with associated velocity vector field along XZ axial cross-section of domain

Figure 10 shows velocity vectors and velocity contours for the cases given in Figs. 7, 8 and 9, in the xy plane at z = 10 cm. These 4 frames show several interesting features. The velocity contours show asymmetry in all 4 frames, unlike the pressure contours in Fig. 8 which shows significant asymmetry only for the V = 7 m/s, S = 0.6 case (Fig. 8.3). However, the velocity field asymmetry is most pronounced in Fig. 10.3 that is from the same run as of Fig. 8.3. The differences in the pressure and velocity asymmetry are likely due to the FLUENT post-processor settings in generating the figures. Resolution of the contours can be controlled by increasing the number of contours in the settings. Figures 7.1, 7.3 and 7.4 have reasonably well-defined core radii, the boundary between the inner core and the outer region where the velocity drops off like in a free vortex. The core radius is not well-defined in Fig. 10.2 for the V = 7.0 m/s, S = 0.6 case. It is evident that through figure 10.3, when S = 2 the region of highest velocity magnitude in red near the ground is the largest in area and in magnitude compared to all other simulations.

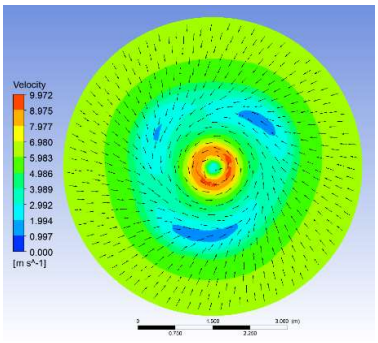

10.1. Run 1, S = 0.2, V = 7.0m/s

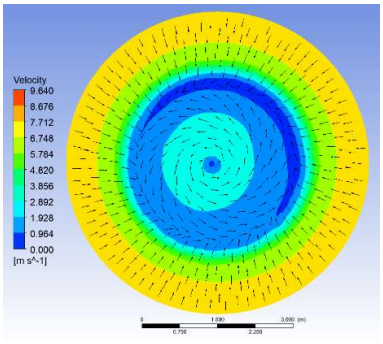

10.2. Run 2, S = 0.6, V = 7.0m/s

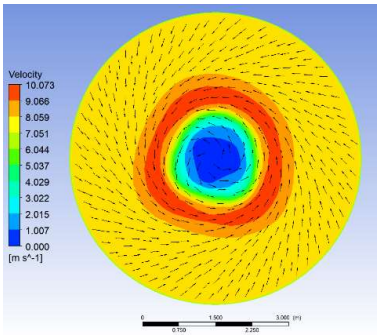

10.3. Run 3, S = 2.0, V = 7.0m/s

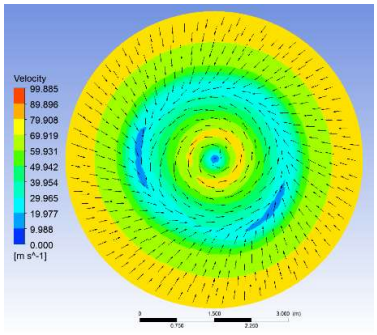

10.4. Run 4, S = 0.6, V = 70.0m/s

Figure 10. Velocity contours with associated velocity vector fields along cross-section of domain at a height of 10cm in the XY plane

Figure 11 shows the pathlines from the 4 cases given in Figs. 7, 8, 9 and 10. Figure 11.1 has 3 main regions: The first (Region 1) is the region close to the ground having low velocities indicated by dark blue. Interior to it is Region 2, where the velocity is higher and has an approximate conical shape. Region 3 is above Region 2, indicated in red, where the pathlines are more densely packed, and the velocity increases having the features of a swirling jet. In Fig. 11.2, the pathline pattern is more complex showing two inner vortices, one near the ground and a second at the top boundary where the velocity is lower. In Fig. 11.3, the inner vortex near the ground is absent and the one near the top boundary takes the shape of a disk on top with a narrow column reaching all the way to the bottom. Figure 11.4 shows the pathlines that are

similar to those in Fig. 11.2, but has a more irregular pattern, probably suggesting a Reynolds number dependence. The inner vortex and the outer flow at the bottom have merged and has a larger radius at the base. The disk with the narrow column has changed its shape, and the narrow column curves up to assume a more complex shape. All the three figures, 7.2, 7.3 and 7.4, have the familiar funnel shape observed in natural tornados.

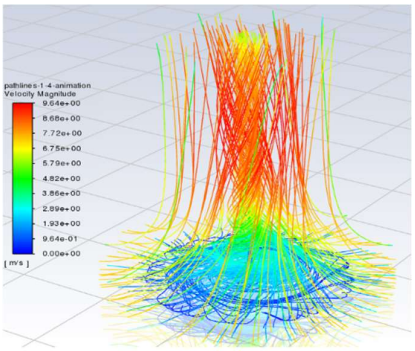

11.1. Run 1, S = 0.2, V = 7.0m/s

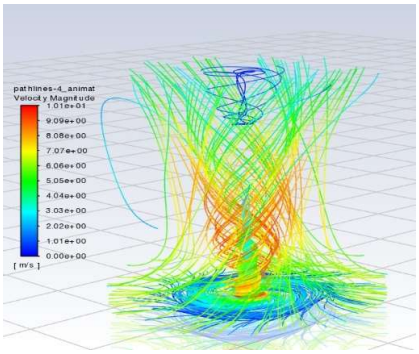

11.2. Run 2, S = 0.6, V = 7.0m/s

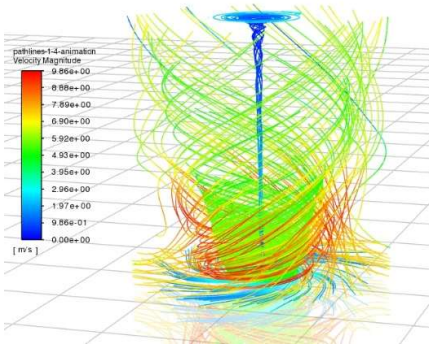

11.3. Run 3, S = 2.0, V = 7.0m/s

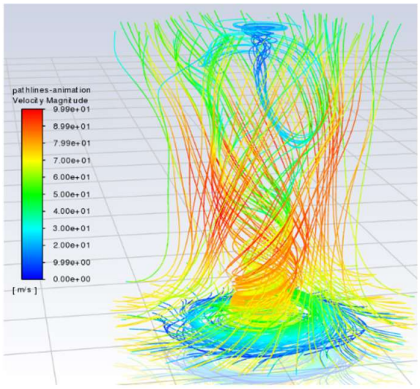

11.4. Run 4, S = 0.6, V = 70.0m/s

Figure 11. Velocity magnitude pathline animation captures showing flow structures

Figure 12 shows the static pressure profile in the radial direction at z = 10 cm for V = 7 m/s and three values of the swirl ratio S = 0.2, 0.6 and 2. It is evident that negative pressure is greatest at S = 0.6 with the shortest width of a negative pressure region. While the pressure at S = 2 although not as large in magnitude, covers a wider width suggesting that the simulation is are well within the vortex breakdown values of S. A noticeable feature is the difference is the difference in the shape of the curve for S = 2 compared to the other two lower values of S. The narrow dip at the center present for the two lower values of S flattens out as S increases to 2. This trend can be explained by also considering the velocity profile that follows.

Figure 13 shows the velocity profiles for the same three values of S as in Fig. 12. A few interesting features are evident in this figure. For S = 0.2 and 0.6 the profiles are similar to the Rankine Combined Vortex (RCV) and the Burger-Rott Vortex (BRV) (Kilty, 2005)[14], showing an inner region where the velocity variation is approximately linear with radius, and the velocity decays at larger radius. The radius where the transition takes place is referred to as the core radius. For these two values of S, the non-dimensional core radius $R/r_0 \simeq 0.1$ where this transition occurs. It is also interesting to note that the highest velocities at the core outskirts are

achieved by the S = 0.6 case. For S = 2, the velocity variation in the core is not linear with one slope, but shows two linear segments, the first having a smaller slope for $0 \le R/r_o \le 0.18$ and the second segment having a larger slope for $R/r_o > 0.18$. The core radius for this case $R/r_o \approx 0.4$.

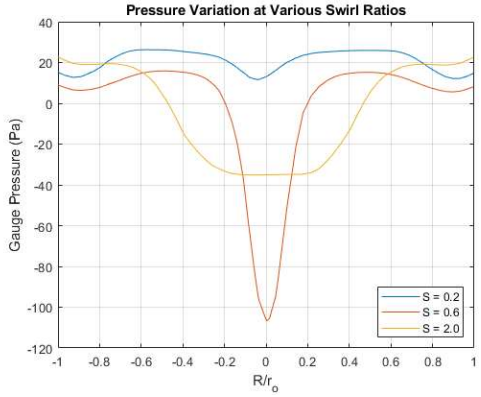

Figure 12. Pressure variation in the radial direction at a height of 10cm in the xy plane for three values of S = 0.2, 0.6 and 2. V_0 = 7 m/s.

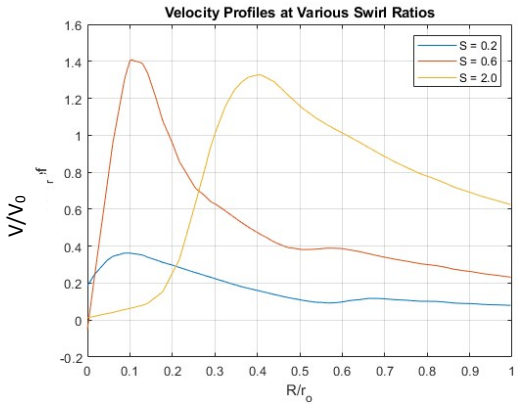

Figure 13. Non-dimensional velocity variation in the radial direction at a height of 10cm in the xy plane for three values of S = 0.2, 0.6 and 2. V_0 = 7 m/s.

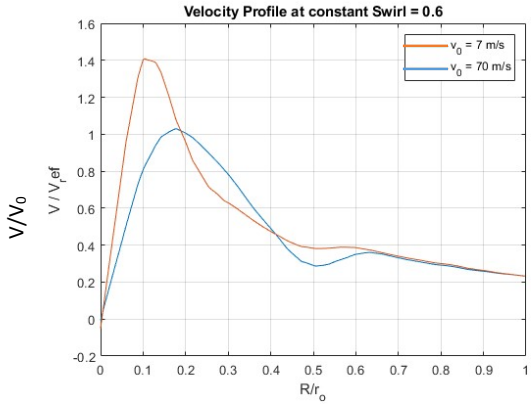

Figure 14. Non-dimensional velocity variation in the radial direction at a height of 10cm in the xy plane for V_0 = 7 m/s and 70 m/s and S = 0.6.

Figure 14 shows the velocity profiles for the two cases V = 7 m/s and 70 m/s. Both show a well-defined core whose radius decreases from $R/r_o \approx 0.18$ for the 70 m/s case to $R/r_o \approx 0.1$ for the 7 m/s case. The decaying outer region has a dip at $R/r_o \approx 0.5$. It is to be noted that the pressure and velocity profiles in Figs. 12, 13 and 14 are close to the ground at z = 10 cm the ground effect can be expected to significantly influence the behavior. At higher elevations, the core region and the outer region can be expected to show different behavior due to the diminished influence of the ground.

3. Conclusions and Ongoing Work

The presented work based on CFD simulations of the flow in a vortex chamber to simulate tornadoes and dust devils shed light into the behavior of such flow fields adding to the knowledge base of them. This expanding knowledge base is critical to the understanding of the genesis and evolution of tornados and dust devils. Computational fluid dynamics has become an essential tool in the investigation of such phenomena. The recent thrust toward Mars exploration highlights the need for such research since dust devils are very common on Mars as evidenced from recent video footage from NASA's Mars vehicles. This work is ongoing with the next phase planned for including the conditions of Mars in the simulations and conducting experiments on the fundamental mechanisms that leading to the formation of tornados and dust devils.

Acknowledgements

A special thank you to Dr. K.M. Isaac for his expertise and knowledge in guiding the CFD research project. This work was supported by NASA Missouri Space Grant Consortium internship to the first author, award number 80NSSC20M0100. The authors thank Missouri S&T for providing office space, lab space and computer access to conduct this research.

Biography

Alexios Philippou grew up between Nicosia, Cyprus, and Boonton, New Jersey, United States, before beginning his college degree, Mechanical Engineering with Aeronautics, at the University of Glasgow in Scotland, UK. He is expected to graduate with an integrated Masters of Engineering (Meng) by the summer of 2024. His interests include space exploration, spaceflight dynamics, additive manufacturing, and extraterrestrial environments. As his career unfolds, he aspires to become involved in the space technology field, working on projects at NASA or similar companies.

References

1. Bluestein, H. B. (2004). Doppler Radar Observations of Dust Devils in Texas. *Monthly Weather Review, 132(1)*, 219-222.
2. Lewellen, W. (1993). Tornado Vortex Theory. In W. Lewellen, *Tornado Vortex Theory. In The Tornado: Its Structure, Dynamics, Prediction, and Hazards,* American Geophysical Union (AGU), pp. 19.
3. Idso, S. (1974). Tornadic Vorticies Spawned By a Desert Brush Fire. *Weather,* pp. 280 - 283.
4. Golden, J. H. (1971). Watersprouts and Tornadoes Over South Florida. *Monthly Weather Review, 99(2)*, pp. 146-154.

5. NASA/JPL-Caltech. (April 13, 2021). *Mars Perseverance Sol 52: Left Navigation Camera (Navcam).*

6. Davies-Jones, R. P. (1976). Laboratory simulations of tornadoes. *Proceedings, Symposium on Tornadoes*, pp. 107-174.

7. Ward, N. B. (1972). The Exploration of Certain Features of Tornado Dynamics using a Laboratory Model. *Journal of the Atmospheric Sciences, 29(6)*, pp. 1194-1204.

8. Lewellen, W. (1962). A solution for three-dimensional vortex flows with strong circulation. *Journal of Fluid Mechanics, 14*, pp. 420 - 432.

9. Davies-Jones, R. P. (1973). The Dependence of Core Radius on Swirl Ratio in a Tornado Simulator. *Journal of Atmospheric Sciences, 30(7)*, pp. 1427-1430.

10. Fiedler, B. H. (1997). Compressibility and windspeed limits in tornadoes. *Atmosphere-Ocean, 35(1)*, pp. 93-107.

11. Xia, J. L. (2003). Influence of Mach Number on Tornado Corner Flow Dynamics. *Journal of the Atmospheric Sciences, 60(22)*, pp. 2820-2825.

12. Rotunno, R. (1979). A Study in Tornado-Like Vortex Dynamics. *Journal of Atmospheric Sciences, 36(1)*, pp. 140-155.

13. Davies-Jones, R. (1986). Thunderstorms morphology and dynamics. *Tornado dynamics*, pp. 197–236.

14. Kilty, K. T. (2005). *Steady-state tornado vortex models,* pp.1-14.